Simultaneous hard X-ray Talbot phase and dark-field imaging in laser experiments at XFEL facilities

V. Bouffetier,[1, a)] M.P. Valdivia,[2] L. Ceurvorst,[3] D. Stutman,[4] G. Rigon,[5] B. Albertazzi,[5] M. Koenig,[5] T. Pikuz,[6] N. Ozaki,[7, 8] H. Nakamura,[7] Y. Hironaka,[8] K. Miyanishi,[9] T. Yabuuchi,[9, 10] T. Togashi,[9, 10] K. Sueda,[9] M. Yabashi,[9, 10] T. Goudal,[11] D. Mancelli,[12] A. Casner,[11] and G. Pérez-Callejo[13]

[1)] *Helmholtz-Zentrum Dresden-Rossendorf (HZDR), D-01328 Dresden, Germany*
[2)] *SLAC National Accelerator Laboratory, Menlo Park, California 94025, USA*
[3)] *Laboratory for Laser Energetics, 250 East River Road, Rochester, NY 14623, USA*
[4)] *ELI-NP, Institute for Physics and Nuclear Engineering, Bucharest-Magurele 077125, Romania*
[5)] *LULI, CNRS, CEA, Ecole Polytechnique, UPMC, Univ Paris 06: Sorbonne Universites, Institut Polytechnique de Paris, F-91128 Palaiseau cedex, France*
[6)] *Institute for Open and Transdisciplinary Research in Initiatives, Osaka University, Osaka 5650871, Japan*
[7)] *Graduate School of Engineering, Osaka University, Osaka 565-0871, Japan*
[8)] *Institute of Laser Engineering, Osaka University, Osaka 565-0871, Japan*
[9)] *RIKEN SPring-8 Center, Hyogo 679-5148, Japan*
[10)] *Japan Synchrotron Radiation Research Institute, Hyogo 679-5198, Japan*
[11)] *CEA, DAM, DIF, F-91297 Arpajon, France*
[12)] *Université de Bordeaux-CNRS-CEA, Centre Lasers Intenses et Applications (CELIA), UMR 5107, F-33405 Talence, France*
[13)] *Departamento de Física Teórica Atómica y Óptica, Universidad de Valladolid, 47011 Valladolid, Spain*

(Dated: 20 November 2025)

X-ray Free Electron Laser (XFEL) facilities offer unprecedented opportunities to advance instrumentation for studying matter under extreme conditions. In this study, we harnessed the enhanced X-ray capabilities of XFELs to demonstrate dark field imaging in laser-driven experiments at XFEL facilities. Utilizing a Talbot X-ray interferometer, we achieved to simultaneously capture transmission, dark-field, and differential phase contrast radiographs of laser-driven metallic foils. Our work showcases the feasibility of single-shot grating-based Talbot X-ray dark field imaging in pump probe experiments at XFEL facilities, opening doors to a wide range of hard X-ray imaging applications in material science and high-energy density physics.

I. INTRODUCTION

X-ray imaging, essential for unveiling the internal structure of matter, often relies on X-ray absorption for contrast, limiting its accuracy in cases of similar absorption coefficients or optically thin samples[1]. Talbot X-ray phase contrast imaging[2] is an approach relying on scattering and phase shifts in the X-ray wavefront to reveal details otherwise concealed[3].

Originally observed in the XIXth century using visible light[4], the Talbot effect consists of the self-imaging of a periodic grating at regular distances given by:

$$d_T = m \cdot \frac{p^2}{2\eta^2\lambda}, \tag{1}$$

when illuminated with coherent light[5–7]. In Eq. 1, p corresponds to the periodicity of the grating, λ is the wavelength of the photons, η is a parameter that depends on the type of the grating[8] and m is an integer number called *the Talbot order*. For absorption gratings, $\eta = 1$ and the Talbot planes (where the self-image is generated) are obtained for even values of m; while for π-shift phase gratings, $\eta = 2$ and the Talbot planes are located at odd values of the Talbot order[8]. In general Talbot designs, a second grating G_2 called *analyzer* is placed at the distance d_T to filter the signal.

An additional advantage of Talbot interferometry is that, on top of the regular phase contrast image, it provides dark-field imaging[3,9], which, by highlighting small-angle X-ray scattering, uncovers micro-structural details such as inhomogeneities and grain boundaries[3,10] often missed by other methods. In material science, dark-field imaging reveals dislocations and internal stresses[11], opening new paths in material design. In biology, it allows for the observation of subcellular entities and nuanced tissue variations[12,13] without external contrasting agents. Developing such methods for laser-generated plasmas could experimentally unveil up-to-now unseen fine-scale structures. This critical point comes to the forefront to understand plasma dynamics[14,15] and hydrodynamic instabilities[16–18].

The main facilities where laser-driven experiments can occur today are dedicated laser facilities such as LULI-2000, OMEGA, GEKKO-XII, NIF or LMJ; or X-ray Free Electron Laser (XFEL) facilities like SACLA[19], LCLS[20], or the European XFEL[21], where all of which have dedicated platforms. These facilities provide a wide range of laser and X-ray conditions that can complement each other.

Typically, laser facilities provide kJ to MJ laser energies, but offer limited X-ray brilliance due to the broadband spectra and divergence of the X-ray source. Previous experiments on the OMEGA-EP laser enabled fringe contrast in the order of 10%[22,23], and a recent study on MTW laser showed that limited laser-driven X-ray source brilliance may strongly constrain the fringe contrast of Talbot X-ray interferometry[24]. On the other hand, the lasers found at XFEL facilities do not currently exceed 100J of energy in the nano-second

[a)] v.bouffetier@hzdr.de

regime but can provide X-ray peak brilliances in the range of $1\times10^{27}-1\times10^{32}$ photon/srad/s/mm^2/0.1%BW thanks to their femtosecond X-ray pulse duration, low divergence, and sharp X-ray spectrum[25–27], thus providing improved capabilities for phase contrast imaging. For this reason, Talbot interferometry experiments at XFEL facilities are becoming more popular[28–30]. Talbot X-ray phase and dark-field imaging coupled to XFEL light emerges as a promising candidate to image laser-matter experiments in the hard X-ray regime.

In this manuscript, we report a primary feasibility study of Talbot X-ray imaging of laser-driven experiments at XFEL facilities, performed at the SACLA XFEL. This work demonstrates the capabilities of Talbot X-ray imaging to provide, in a single shot, transmission, phase difference and dark-field radiographs in this type of experiments.

The manuscript is structured as follows. In Section II, we present some fundamentals on the theory of Talbot imaging and discuss the physical magnitudes that can be obtained from an experiment of this type. Section III describes the experimental setup that was used in our particular case, and Section IV shows the obtained experimental results. Finally, in Section V we present a brief summary of the conclusions of this work and future perspectives of Talbot imaging at XFEL facilities.

II. SIGNAL DEPENDENCIES IN TALBOT IMAGING

As mentioned above, in Talbot interferometry experiments, the self-image of a periodic grating is recorded onto a detector as a collection of fringes. Generally, a sample object is placed on the radiation path to observe its effect on the measured pattern. From the fringe analysis of Talbot patterns, one can extract up to three different images related to different aspects of the interaction of the X-rays probing a sample, while absorption imaging and free propagation phase contrast imaging provide one and two different sets of information, respectively.

The first image that can be retrieved from Talbot interferograms is the *transmission* image, which is related to the variation of the illumination function due to the absorption of the X-rays by the sample, similarly to absorption imaging. The second image is the *phase difference* image, resulting from the difference between the phase of the interferogram perturbed by the sample, and the phase of the unperturbed Talbot pattern (when no sample has been placed on the path of the X-rays). This phase difference of the fringes is directly proportional to the phase gradient on the perturbed X-ray wavefront, which is why it is often referred to in the literature as the phase gradient image. The last image is the *dark-field* radiograph. This radiograph is the result of the change of the visibility of the fringes composing the Talbot pattern due to small angle X-ray scattering induced by a sample.

In general, the Talbot fringe pattern can be written as:

$$S = A(x,y) + B(x,y)\sin\left[\phi(x,y)\right]. \tag{2}$$

The transmission (T), phase difference ($\Delta\phi$), and dark-field (DF) images can then be expressed as

$$T = \frac{A_{\text{Perturbed}}}{A_{\text{Ref}}}, \tag{3}$$

$$\Delta\phi = \phi_{\text{Perturbed}} - \phi_{\text{Ref}}, \tag{4}$$

$$DF = \frac{B_{\text{Perturbed}}}{B_{\text{Ref}}}\cdot\frac{A_{\text{Ref}}}{A_{\text{Perturbed}}} = \frac{V_{\text{Perturbed}}}{V_{\text{Ref}}}, \tag{5}$$

where the indices 'Perturbed' and 'Ref' respectively indicate the signals of the interferogram acquired with and without a sample perturbing the Talbot pattern and $V = B/A$ is the fringe *visibility*. In this work, we made use of the Fourier-based TIA Talbot Numerical Tool (TIA/TNT) code[23,31,32] to isolate the mean illumination component (A) from the fringe amplitude (B) and fringe's phase (ϕ) and obtain these images. A detailed description of the operation of TIA/TNT can be found in Pérez-Callejo *et al.*[23,31,33].

These three images contain different physical information about the sample. For the transmission image,

$$T = \exp\left(-\mu l\right), \tag{6}$$

where μ is the linear absorption coefficient of the sample and l is the thickness of the sample.

In the case of the phase, one can write:

$$\Delta\phi = \frac{\lambda d_T}{p_2}\cdot\frac{\partial\varphi}{\partial x} \tag{7}$$

where x is the direction perpendicular to the fringes, p_2 is the period of the analyzer, and φ is the phase of the perturbed X-ray wavefront. This can be written in terms of the optical properties of the material as

$$\varphi = \frac{2\pi}{\lambda}\int\delta dz \tag{8}$$

where z is the direction along the X-ray beam, and δ is the real part of the optical index. In the cold approximation, δ can be expressed by[34]:

$$\delta = \frac{r_e\lambda^2}{2\pi}n_e \tag{9}$$

with r_e is the classical electron radius and n_e the electron density. This retrieves the fact that the phase difference image in Talbot interferometry is directly proportional to the integrated electron density gradient in the sample:

$$\Delta\phi \propto \frac{\partial\varphi}{\partial x} \propto \frac{\partial}{\partial x}\int n_e dz. \tag{10}$$

In the case of hot and dense plasmas, where atomic states are more exotic, more complicated models need to be considered[31,35,36].

Dark-field imaging measures the fringe's visibility change directly related to the width of the total scattering angular width σ from the sample as[37]

$$DF = \exp\left(\frac{-2\pi^2}{p_2^2}\sigma^2 d_{SG_2}^2\right), \tag{11}$$

where d_{SG_2} is the sample to analyzer distance, and σ is the scattering width, related to the linear diffusion coefficient ε of the sample by:

$$\varepsilon\, l = \sigma, \tag{12}$$

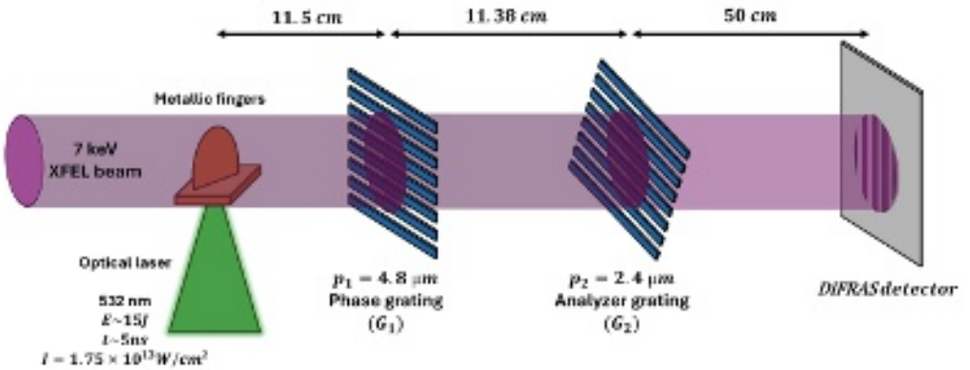

FIG. 1. Experimental setup: a 532 nm wavelength laser with 15 J energy and 5 ns square temporal profile irradiate a 10 µm thick metalic foil with 10° incidence and 180 µm FWHM focal spot. The metallic foil is then imaged using a 7 keV XFEL beam collimated with 1 mm FWHM diameter coupled with a two grating Talbot interferometer, and images are recorded using the DIFRAS X-ray detector.

where, same as in Eqn. 6, l is the thickness of the sample. Given that the scattering width is strongly connected to the scattering vectors q (as discussed in recent literature[38–42]), dark-field image is an additional diagnostic, complementary to small angle X-ray scattering.

III. EXPERIMENTAL SETUP

A. Samples and laser parameters

In Fig.1, we depict the experimental configuration employed at employed at the BL3-EH5 of SACLA[43,44]. The samples used during the experiment were copper and aluminium foils of 10 µm thickness. The targets were irradiated by a laser with wavelength $\lambda_L = 532$ nm and pulse duration of 5 ns. The laser beam was focused into a spot size of 180 µm FWHM to reach a total intensity of $I_L = 1.75 \times 10^{13}$ W cm^{-2}. To avoid risk of back reflection from the laser, the normal of the foils' surface was angled at 10° to the laser axis .

B. Imaging platform

To image the evolution of the samples, we used a collimated X-ray beam with a diameter of 1 mm and photon energy of 7 keV ($\lambda = 1.77$ Å). The X-ray beam had a pulse duration of 7 fs and an energy of 700 µJ per pulse.

For X-ray interferometric measurements, we assembled a compact two-grating Talbot interferometer. The diagnostic comprises a π-shift phase grating of period $p_1 = 4.8$ µm, which we will refer to as *beamsplitter*, and an absorption grating of period $p_2 = 2.4$ µm, hereafter referred to as the *analyzer* (as mentioned in Section I), each of them with a working area of 5 mm diameter. The gratings were separated by a distance of $d_T = 11.38$ cm, corresponding to a Talbot order of $m = 7$ for the X-ray wavelength used, as shown in Eqn. 1. The angular sensitivity of the interferometer is $S = p_2/d_T = 21.09$ µrad[8].

The Diffusion-free transparent scintillator (DIFRAS) X-ray

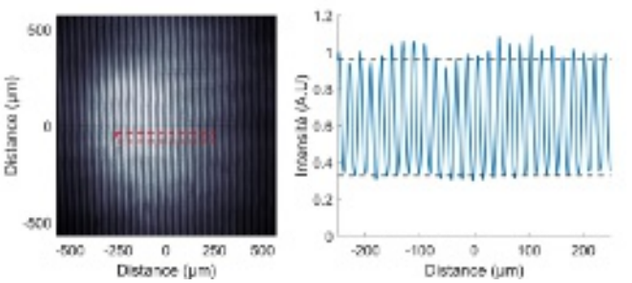

FIG. 2. Experimental interferogram: Raw interferogram (left) and fringe profile after normalization by the illumination function (right). The observed local variations of the fringe contrast are the result of the grating imperfections resulting in slight changes in the gratings' efficiency.

detector[45,46] used during the experiment was placed 50 cm after the analyzer grating (i.e. 70 cm from the target chamber center). This X-ray detector consists in a LuAG scintillator[45] coupled to optical magnification, thus enabling a millimetric field of view of 1.33×1.33 mm^2 over a 2048×2048 pixels chip with effective pixel size of 0.65 µm.

C. X-ray peak brilliance of the source

As mentioned above, we used 7 keV photons with 700 µJ/pulse using 7 fs pulses. This provided a photon statistic of 6.25×10^{11} photon/pulse available for single shot radiography events. To obtain the peak brilliance of the X-ray source, we note that the divergence of the XFEL beam at the BL3 of SACLA is of the order of the microradian[43,47]. Furthermore, according to previous studies, the X-ray source size at the BL3-EH5 is on the order of 60 µm[48,49]. Additionally, the X-ray bandwidth at 7 keV is ~ 26 eV. These numbers yield an estimated peak brilliance of the X-ray source during our experiment of $B = 2.9 \times 10^{31}$ photons/mrad^2/mm^2/s/0.1%BW.

For comparison with recent Talbot imaging experiment car-

ried at OMEGA-EP laser[22,23], let us do an estimation of the brilliance of X-ray sources produced at these type of laser facilities. The photon energy closest to our case (7 keV) which can be obtained with a short pulse laser-driven X-ray source is the K-α emission of cobalt ($E_{k\alpha,Co} = 6.93\,\mathrm{keV}$). The typical pulse duration used at the OMEGA-EP laser for producing K-α sources is on the order of $10-100\,\mathrm{ps}$, with a maximum available energy in the short-pulse laser beam of 2.3 kJ (for 100 ps pulse duration), and a laser intensity on the order of $1\times10^{18}\,\mathrm{W/cm^2}$ (corresponding to a diameter of the focal spot of 40 µm). According to Park *et al.*[50], the conversion from laser to K-α emission expected for this intensity regime is on the order of $\varepsilon = 1\times10^{-5}$, leading to a 2.07×10^{13} K-α photons. Since the life-time of laser-generated X-ray sources is approximately that of the duration of the laser pulse (100 ps), assuming that the emission diverges over 2π srad, and has a bandwidth of $\sim 100\,\mathrm{eV}$, the brilliance of such source would then be approximately $B_{laser} = 3.7\times10^{17}\,\mathrm{photons/mrad^2/mm^2/s/0.1\%BW}$.

It is therefore clear that, with nearly 14 orders of magnitude higher brilliance, coherent X-ray imaging methods are better suited to be used in combination with XFEL sources, even if the total amount of photons in a single pulse is two orders of magnitude lower than in the case of laser-driven X-ray sources. These differences translate to a factor of 5 lower fringe contrast observed at the OMEGA-EP laser[23], with respect to the one referenced in this manuscript in Fig.2.

D. Spatial resolution

The spatial resolution of a Talbot interferometer is limited by different factors. The first limitation comes from the the X-ray detector, which in our case limits the resolution to $\sim 2\,\mu\mathrm{m}$ considering the potential spreading of the energy of an incident photon on the CCD to the pixel's first neighbors. Secondly, the resolution of a Talbot interferometer when using a collimated X-ray beam cannot be better than twice the analyzer grating period, which in our case translates to 4.8 µm. Finally, the spatial resolution of the diagnostic is limited by the shear length enabled by the diagnostic, which, for our design was $L_S = 4d_T\lambda/p_1 = 16.8\,\mu\mathrm{m}$[51] and therefore constitutes the resolution limit of our diagnostic. While using a lower Talbot order would enable a higher spatial resolution thanks to the reduced intergrating distance d_T, this enhanced resolution would come to the cost of angular sensitivity, critical for dark-field signal.

An additional limitation to spatial resolution that needs to be taken into account is motion blur. This contribution is independent of the interferometer design, and depends exclusively on the duration of the X-ray pulse and the velocity of the system that is being imaged. While this contribution is non-negligible when laser-produced X-ray sources are used, we note that, in our case, the duration of the X-ray pulse is τ_{X-ray}=7 fs, and, therefore, the maximum limitation to spatial resolution caused by this effect is $\sim c\tau_{X-ray} \sim 2\,\mu\mathrm{m}$, which is significantly below the 16.8 µm limitation imposed by the interferometer design. The actual motion blur contribution to the images in this particular experiment is discussed in more detail in the following section. As a consequence, the main imaging resolution limitation from this experimental platform comes nor from the motion blur, nor from the detector but from the Talbot grating interferometer's shear length itself.

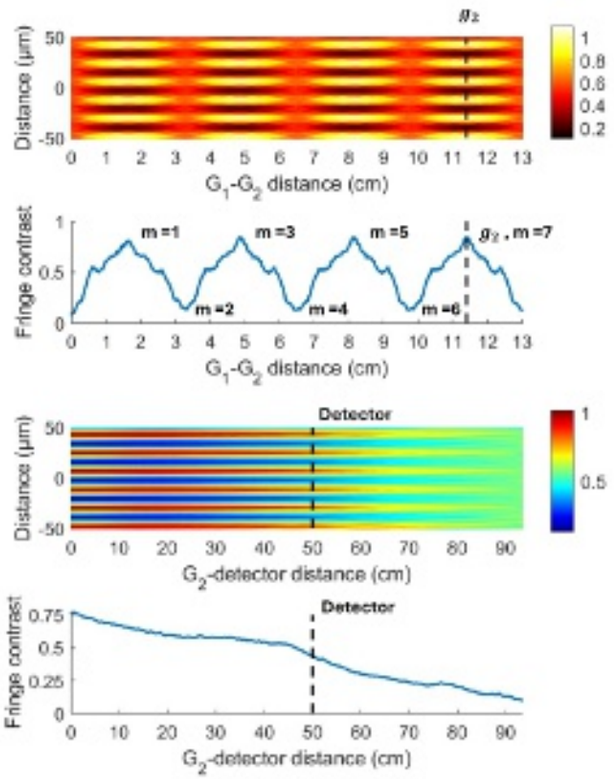

FIG. 3. Simulation of the grating interferometer's fringe pattern using the TIA code: (a) Normalized fringe pattern 1 mm after the analyzer grating (G_2) as a function of the G_1-G_2 distance, and (b) associated fringe visibility curve as function of the intergrating distance. (c) Shows the evolution of the normalized fringe pattern as function of the $G_2-detector$ distance, and (d) shows in blue the evolution of the fringe contrast over distance after G_2.

IV. EXPERIMENTAL RESULTS

A. Fringe properties

To resolve the periodicity of the fringes, we rotated the analyzer grating with respect to the beamsplitter by an angle $\theta = 7.5°$, which generated a larger Moiré pattern with a periodicity of $F = p_2/(2\sin(\theta/2)) \approx 18\,\mu\mathrm{m}$. The raw fringe pattern obtained with a single X-ray shot is displayed on the left of Fig.2. After correcting the radiograph by normalizing it with the XFEL spot shape, we extracted a line profile from the center of the red box drawn on the fringe pattern, which is shown on the right of Fig.2. This line profile exhibits a fringe contrast of $C = (I_{max}-I_{min})/(I_{max}+I_{min}) = 49.6\,\% \pm 1.5\,\%$. The fluctuations of the fringes' amplitude are related to defects in the gratings' micro-structures thus slightly altering the local fringe contrast.

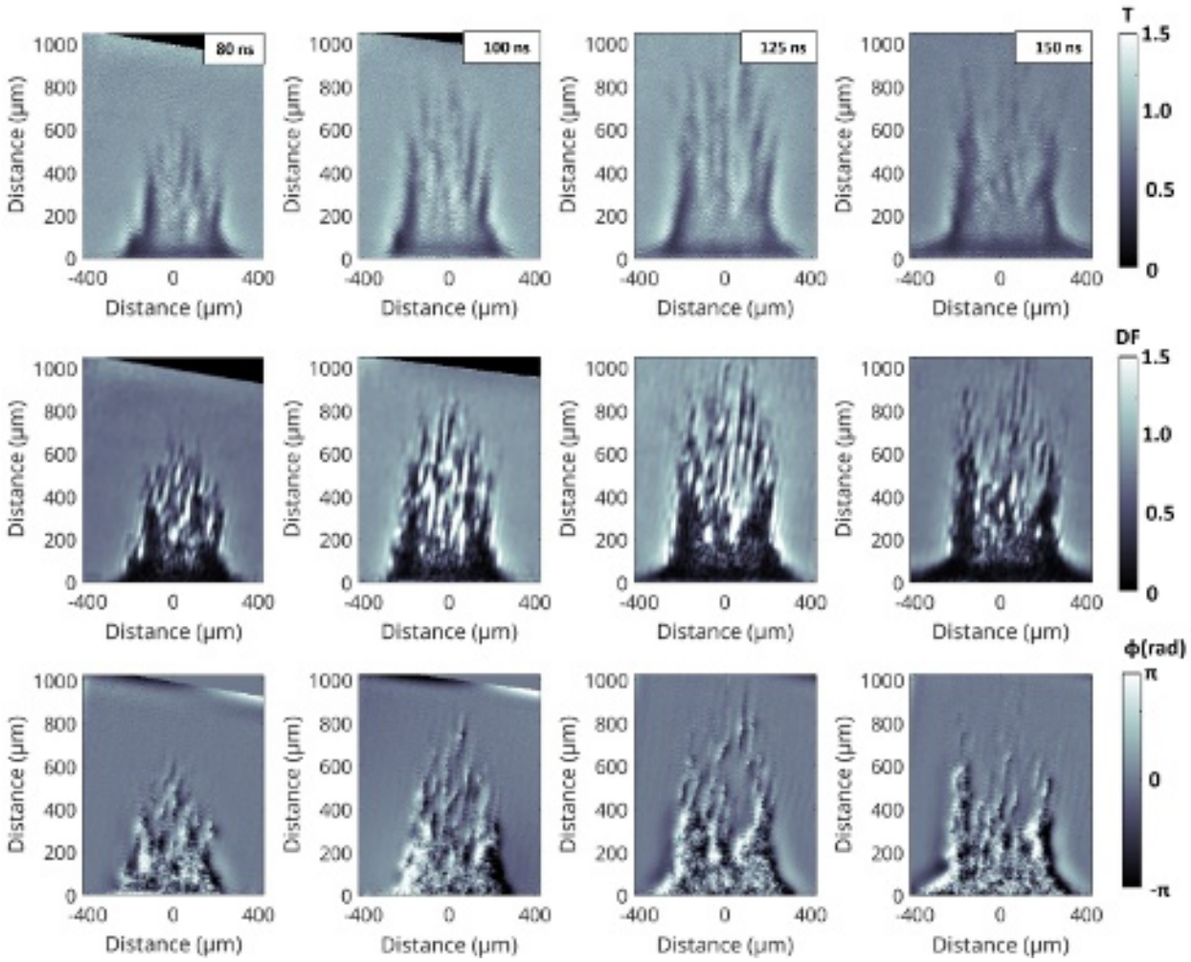

FIG. 4. Single shot Transmission (top line), dark-field (middle line), and interferogram phase difference (bottom line) radiographs of rear side copper ejections at $t = 80 - 150$ ns. The four presented pictures come from different foils which have been irradiated with similar laser parameters. Additionally, each radiograph has been obtained using a single XFEL pulse

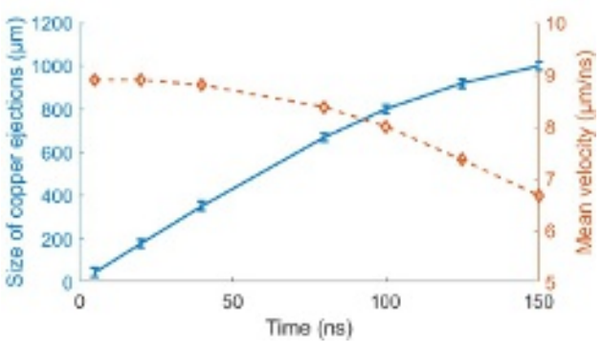

FIG. 5. Time evolution of the maximum copper finger size other time in blue, and time evolution of the mean velocity of the copper ejection in orange.

We used the TIA code[31] to compare experimental properties of the obtained fringe pattern to theory. TIA is a Fourier-based wave-propagation code designed to model Talbot interferometry experiments. While TIA is optimized to work with plane waves, rather than Gaussian beams, owing to the high coherence of the X-ray beam used in this experiment, the planar wave assumption provides sufficient accuracy.

In Fig.3.(a), we show the expected fringe pattern (vertical axis) right after the second grating (G_2) as a function of the distance between the gratings (horizontal axis), while Fig.3.(b) shows the corresponding fringe contrast. We can see that, as expected, the maximum contrast is obtained for integrating distances of ~ 1.63, 4.88, 8.14 and 11.39 cm, corresponding to the $m = 1, 3, 5$ and 7 Talbot orders. It can be seen that, if the X-ray detector was placed right after the analyzer grating, the expected fringe pattern for the $m = 7$ Talbot order would be $\sim 76\,\%$ with ideal gratings. However, as mentioned above, owing to geometrical constraints from the experimental station, the X-ray detector was placed 50 cm away from the analyzer. For this reason, we evaluated the evolution of the fringe contrast as function of the detector distance for a span of

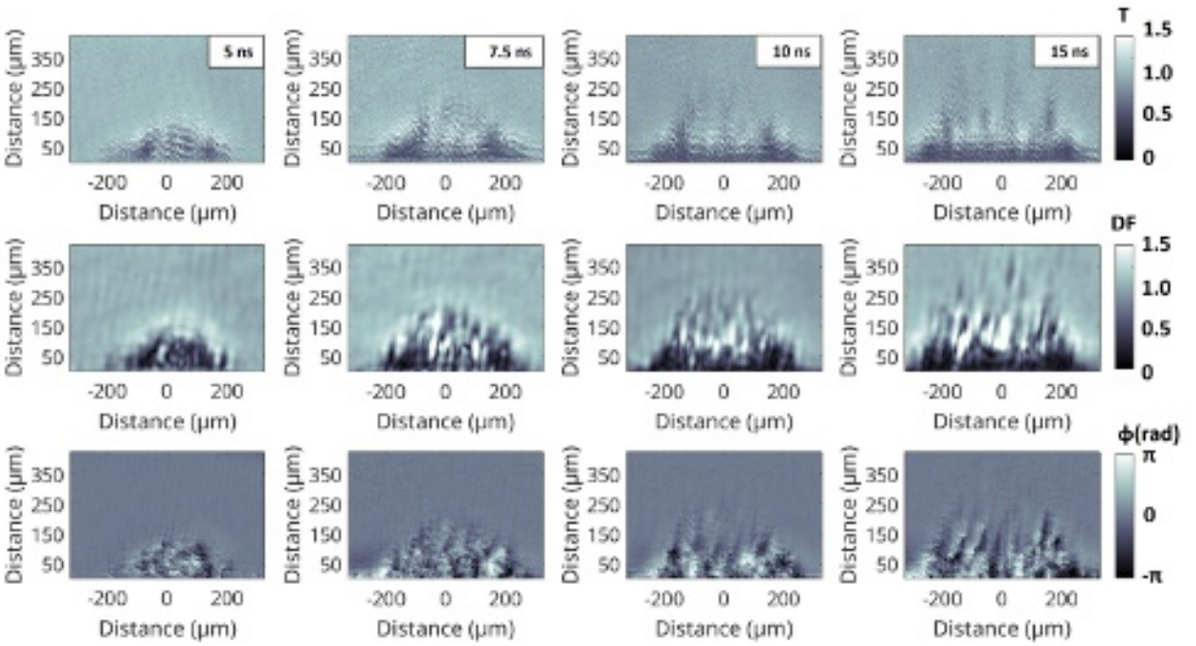

FIG. 6. Single shot Transmission (top line), dark-field (middle line), and interferogram phase difference (bottom line) radiographs of rear side Aluminum ejections at $t = 5 - 15$ ns. The four presented pictures come from different foils which have been irradiated with similar laser parameters. Additionally, each radiograph has been obtained using a single XFEL pulse.

90 cm. This pattern is shown in Fig.3.(c), with Fig.3.(d) being the corresponding fringe contrast. We can observe that, within this range, the further away the detector is from the analyzer, the lower the fringe contrast becomes. The expected contrast at our experimental distance of 50 cm is $\sim 46\,\%$, which is in perfect agreement with the fringe contrast measured in the experiment (as shown in Fig. 2).

Additionally, Fig.3.(d), shows that the maximum fringe contrast of the interferometer (76%) is obtained right after the analyzer grating. After G_2, the contrast then rapidly decreases to $\sim 60\,\%$ in the first 20 cm after the grating. It is then expected to stabilize around this value up to a distance of 40 cm after G_2, before continuously decreasing down to 10 % between 40 cm and 90 cm. Importantly, this shows that, if the geometrical constraints of the facility impose a distance of the X-ray detector $20 - 40$ cm after the analyzer this may not impact strongly the fringe properties under collimated illumination with XFEL light[1].

[1] The authors want to highlight that this statement is only valid in the case of a beamsplitter coupled to analyzer Talbot interferometer such as the one used in this work. In the case where only a Talbot phase grating is used, the distance between the Talbot grating and detector must strictly correspond to one of the Talbot planes to optimize the fringe contrast which would be strongly affected otherwise (as shown in Fig.3.(a). This therefore hints that 2-gratings Talbot diagnostics might be more resilient than single gratings setups when the detectors' position is restricted.

B. Imaging results of metallic foils ejections

When the 532 nm laser irradiates the samples in this experiment, the abrupt energy deposition from the laser to the foil launches a strong shock into the metal. When the shock breaks out from the rear surface of the metallic foils, liquid ejections can be observed (cf. Fig.4 and Fig.6).

In Fig.4 we present imaging results of the copper foils at probe times of $80 - 150$ ns. We show image reconstruction of the transmission (first line), dark-field (second line) and phase difference (third line) obtained from single shot X-ray Talbot interferograms using the TIA/TNT code[23,32]. Each image shown in this figure is obtained from a different laser shot on a different copper foil. Since the targets were all flat foils, the consistency of the observed jet structure shot-to-shot is attributed to the imprint of the laser on the copper foils as seed of the ejections.

The ejection of melted material from the copper foils is clearly observed in the images, which allows us to obtain information from the morphological aspects of the liquid ejection, and measure the dynamic evolution of the copper ejection. This is presented in Fig. 5, where we show the time evolution of the maximum finger size and their mean velocity as a function of time.

Coming back to the motion blur effect mentioned in Section III, it can be seen that the velocity of the copper liquid ejection is of the order of $10\,\mu\mathrm{m/ns}$. With a 7 fs time integration from the X-ray pulse length, the impact of the motion blur on the radiograph is estimated to be $\mathrm{res}_{\mathrm{motion,XFEL}} = 0.07$ nm. Given that this is below the X-ray wavelength used during the

experiment, the motion blur can be considered negligible in these conditions.

Below the filamentary structures of copper, although the transmission is still relevant, the visibility of the fringes drops to zero (as seen in the dark-field image), causing the phase shift to saturate after reaching a full phase shift jump of 2π. This phase saturation reduces the quantitative phase information that can be extracted in this particular case. Similarly, as the dark field signal goes down to zero, quantitative analysis using Eq.11 is not possible in this experiment.

The equivalent imaging results for aluminum foils are shown in Fig.6. In this case, while transmission levels are higher than in copper, the scattering component still highly impacts the fringe visibility of the interferogram, thus resulting in a strong dark field component. Since in this configuration dark field imaging becomes the most sensitive signal, we can clearly observe the formation of cracks turning into filamentary ejections in the aluminum bump at $t = 5$ ns and the formation of aluminum drops due to the stretching of the aluminum fingers at times greater than 7.5 ns. These dynamic effects are not resolved in the transmission images due to the lower sensitivity of transmission compared to dark field. This shows that, at equal resolution, the dark field imaging modality has the potential to provide improved imaging sensitivity for spallation and impact physics in laser-driven experiments.

V. CONCLUSION AND PERSPECTIVES

In this manuscript, we demonstrate for the first time the simultaneous retrieval of transmission, phase and dark-field images from Talbot interferometry in the frame of pump-probe experiments at XFEL facilities.

Since Talbot interferometry is a recent diagnostic development at XFEL facilities[28,29], we provide imaging dependencies to connect the produced radiographs to the different interactions of X-rays with matter.

The measured interferometric parameters are compared with TIA, a Fourier based X-ray propagation code. TIA shows remarkable agreement with the observed fringe pattern, and the experimental fringe contrast is well reproduced. These predictions can be used to improve existing experimental platforms.

Timeline reconstruction of images has been performed showing the reproducibility of the method to understand laser-driven dynamics, proved by the measurements of the copper ejecta filaments. We show that dark field imaging carries improved image sensitivity, and can allow one to observe details unseen in regular transmission or phase images.

Ways of optimization of the platform are proposed to further improve imaging quality in future experiments. This work paves the way for future hard X-ray imaging techniques at hard XFEL facilities enabling simultaneous absorption, phase, and small angle X-ray scattering (dark-field) single-shot imaging. By building on this platform in future work, dark field could provide improved plasma description when combined with transmission and phase. More generally, dark field imaging has the potential to provide increased sensitivity and information in porous media[52]. This capability could therefore provide novel insights in future studies of laser driven foams to improve our understanding of foam homogenization and hydrodynamic instabilities.

Further improvement of the platform could be obtained by working on reducing the detector to sample distance, or using shorter grating and fringe periods to increase the spatial resolution. This could enable the study of Rayleigh-Taylor and Kelvin-Helmholtz instabilities[53,54] for which this platform is a preliminary testbed.

Additionally, improved phase and dark field imaging could be obtained using 2D grating structures instead of the 1D line gratings shown here. Therefore, checkerboard[55] or circular gratings[56] could improve the imaging quality by increasing the number of scattering directions that the diagnostic is sensible to.

ACKNOWLEDGEMENTS

The XFEL experiment was performed at the BL3-EH5 of SACLA with the approval of the Japan Synchrotron Radiation Research Institute (JASRI) (Proposal No. 2021A8623). The results were obtained using a high-power nanosecond laser deployed at SACLA by Institute of Laser Engineering of Osaka University.

The authors would like to acknowledge for funding and support: the Conseil Régional Aquitaine (INTALAX); the Agence Nationale de la Recherche (ANR-10-IDEX-03-02, ANR-15-CE30-0011), US Department of Energy - National Nuclear Security Administration - High Energy Density Laboratory Plasmas DE-NA0001835, DE-NA0002955, and DE-NA0003882. This work has also been supported by Research Grant No. PID2022-137632OB-I00 from the Spanish Ministry of Science and Innovation.

The work of G.P.-C. has also been carried out within the framework of the EUROfusion consortium, funded by the European Union via the Euratom Research and Training Program (Grant Agreement Nos. 633053 and 101052200—EUROfusion). This work was financially supported by grants from JSPS KAKENHI (Grant Nos. 22K18702 and 23K20038), JSPS Core-to-Core program (JPJSCCA20230003), and MEXT Q-LEAP (JPMXS0118067246 and JP-MXS0118070187). D. Mancelli acknowledges financial support from the French government in the framework of the University of Bordeaux's France 2030 program / GPR LIGHT.

DISCLOSURES

The authors declare no conflict of interest.

DATA AVAILABILITY

The data underlying the results presented in this manuscript are not publicly available at this time but may be obtained from

the authors upon request.

[1]M. Riedel, K. Taphorn, A. Gustschin, M. Busse, J. U. Hammel, J. Moosmann, F. Beckmann, F. Fischer, P. Thibault, and J. Herzen, Scientific Reports **13**, 6996 (2023).
[2]F. Pfeiffer, T. Weitkamp, O. Bunk, and C. David, Nature physics **2**, 258 (2006).
[3]F. Pfeiffer, M. Bech, O. Bunk, P. Kraft, E. F. Eikenberry, C. Brönnimann, C. Grünzweig, and C. David, Nature materials **7**, 134 (2008).
[4]H. F. Talbot, The London, Edinburgh, and Dublin Philosophical Magazine and Journal of Science **9**, 401 (1836).
[5]L. Rayleigh, The London, Edinburgh, and Dublin Philosophical Magazine and Journal of Science **11**, 196 (1881).
[6]A. Momose, S. Kawamoto, I. Koyama, Y. Hamaishi, K. Takai, and Y. Suzuki, Japanese journal of applied physics **42**, L866 (2003).
[7]A. Momose, Optics express **11**, 2303 (2003).
[8]T. Donath, M. Chabior, F. Pfeiffer, O. Bunk, E. Reznikova, J. Mohr, E. Hempel, S. Popescu, M. Hoheisel, M. Schuster, *et al.*, Journal of Applied Physics **106** (2009).
[9]T. Michel, J. Rieger, G. Anton, F. Bayer, M. W. Beckmann, J. Durst, P. A. Fasching, W. Haas, A. Hartmann, G. Pelzer, *et al.*, Physics in Medicine & Biology **58**, 2713 (2013).
[10]T. H. Jensen, M. Bech, O. Bunk, T. Donath, C. David, R. Feidenhans, and F. Pfeiffer, Physics in Medicine & Biology **55**, 3317 (2010).
[11]C. Yildirim, C. Jessop, J. Ahlström, C. Detlefs, and Y. Zhang, Scripta Materialia **197**, 113783 (2021).
[12]M. Töpperwien, M. Krenkel, D. Vincenz, F. Stöber, A. M. Oelschlegel, J. Goldschmidt, and T. Salditt, Scientific reports **7**, 42847 (2017).
[13]M.-C. Zdora, J. Vila-Comamala, G. Schulz, A. Khimchenko, A. Hipp, A. C. Cook, D. Dilg, C. David, C. Grünzweig, C. Rau, *et al.*, Biomedical optics express **8**, 1257 (2017).
[14]W. Amatucci, Journal of Geophysical Research: Space Physics **104**, 14481 (1999).
[15]K. Lotov, A. Pukhov, and A. Caldwell, Physics of Plasmas **20** (2013).
[16]A. Spicher, K. Deshpande, Y. Jin, K. Oksavik, M. D. Zettergren, L. B. Clausen, J. I. Moen, M. R. Hairston, and L. Baddeley, Journal of Geophysical Research: Space Physics **125**, e2019JA027734 (2020).
[17]G. Rigon, B. Albertazzi, T. Pikuz, P. Mabey, V. Bouffetier, N. Ozaki, T. Vinci, F. Barbato, E. Falize, Y. Inubushi, *et al.*, Nature communications **12**, 2679 (2021).
[18]A. Casner, Philosophical Transactions of the Royal Society A **379**, 20200021 (2021).
[19]K. Tono, T. Togashi, Y. Inubushi, T. Katayama, S. Owada, T. Yabuuchi, A. Kon, I. Inoue, T. Osaka, H. Yumoto, *et al.*, in *Advances in X-ray Free-Electron Lasers Instrumentation IV*, Vol. 10237 (SPIE, 2017) p. 1023706.
[20]C. Bostedt, S. Boutet, D. M. Fritz, Z. Huang, H. J. Lee, H. T. Lemke, A. Robert, W. F. Schlotter, J. J. Turner, and G. J. Williams, Reviews of Modern Physics **88**, 015007 (2016).
[21]T. Tschentscher, C. Bressler, J. Grünert, A. Madsen, A. P. Mancuso, M. Meyer, A. Scherz, H. Sinn, and U. Zastrau, Applied Sciences **7**, 592 (2017).
[22]M. Valdivia, D. Stutman, C. Stoeckl, W. Theobald, G. Collins, V. Bouffetier, M. Vescovi, C. Mileham, I. Begishev, S. Klein, *et al.*, Review of Scientific Instruments **92** (2021).
[23]G. Pérez-Callejo, V. Bouffetier, L. Ceurvorst, T. Goudal, S. R. Klein, D. Svyatskiy, M. Holec, P. Perez-Martin, K. Falk, A. Casner, and et al., High Power Laser Science and Engineering **11**, e49 (2023).
[24]V. Bouffetier, G. Pérez-Callejo, D. Stutman, C. Stoeckl, I. Begishev, W. Theobald, T. Filkins, C. Mileham, L. Ceurvorst, S. Klein, *et al.*, Optics express **32**, 34694 (2024).
[25]A. Halavanau, F.-J. Decker, C. Emma, J. Sheppard, and C. Pellegrini, Journal of synchrotron radiation **26**, 635 (2019).
[26]R. Khubbutdinov, N. Gerasimova, G. Mercurio, D. Assalauova, J. Carnis, L. Gelisio, L. Le Guyader, A. Ignatenko, Y. Y. Kim, B. E. Van Kuiken, *et al.*, Structural Dynamics **8** (2021).
[27]I. Inoue, T. Osaka, T. Hara, T. Tanaka, T. Inagaki, T. Fukui, S. Goto, Y. Inubushi, H. Kimura, R. Kinjo, *et al.*, Nature photonics **13**, 319 (2019).
[28]V. Bouffetier, *Développement de l'interférométrie X et application à l'imagerie par contraste de phase de plasmas denses et turbulents*, Ph.D. thesis, Université de Bordeaux (2021).
[29]E. Galtier, H. J. Lee, D. Khaghani, N. Boiadjieva, P. McGehee, A. Arnott, B. Arnold, M. Berboucha, E. Cunningham, N. Czapla, *et al.*, Scientific Reports **15**, 7588 (2025).
[30]C. Parisuaña, M. Valdivia, V. Bouffetier, K. Kurzer-Ogul, G. Perez-Callejo, S. Bott-Suzuki, A. Casner, N. S. Christiansen, N. Czapla, D. Eder, *et al.*, Physics of Plasmas **32** (2025).
[31]G. Pérez-Callejo, V. Bouffetier, L. Ceurvorst, T. Goudal, M. Valdivia, D. Stutman, and A. Casner, Physics of Plasmas **29** (2022).
[32]M. P. Valdivia, G. Pérez-Callejo, L. Izquierdo, F. Veloso, A. Truong, H. Hu, N. Dilworth, S. C. Bott-Suzuki, and V. Bouffetier, IEEE Transactions on Plasma Science , 1 (2024).
[33]G. Pérez Callejo, V. Bouffetier, D. Zulevic, M. Makita, M. Koenig, B. Albertazzi, M. Vescovi, P. Mercere, P. Dasilva, T. Pikuz, *et al.*, In preparation (2025).
[34]A. Momose, W. Yashiro, Y. Takeda, Y. Suzuki, and T. Hattori, Japanese journal of applied physics **45**, 5254 (2006).
[35]G. Williams, H.-K. Chung, S. Vinko, S. Künzel, A. Sardinha, P. Zeitoun, and M. Fajardo, Physics of Plasmas **20** (2013).
[36]K. Wiesemann, arXiv preprint arXiv:1404.0509 (2014).
[37]M. Bech, O. Bunk, T. Donath, R. Feidenhans, C. David, and F. Pfeiffer, Physics in Medicine & Biology **55**, 5529 (2010).
[38]A. Ritter, P. Bartl, F. Bayer, K. C. Gödel, W. Haas, T. Michel, G. Pelzer, J. Rieger, T. Weber, A. Zang, *et al.*, Optics express **22**, 23276 (2014).
[39]K. S. Morgan and D. M. Paganin, Scientific reports **9**, 17465 (2019).
[40]M. Strobl, Scientific reports **4**, 7243 (2014).
[41]F. T. Gassert, T. Urban, M. Frank, K. Willer, W. Noichl, P. Buchberger, R. Schick, T. Koehler, J. von Berg, A. A. Fingerle, *et al.*, Radiology **301**, 389 (2021).
[42]T. Urban, F. T. Gassert, M. Frank, K. Willer, W. Noichl, P. Buchberger, R. C. Schick, T. Koehler, J. H. Bodden, A. A. Fingerle, *et al.*, Radiology **303**, 119 (2022).
[43]K. Tono, T. Togashi, Y. Inubushi, T. Sato, T. Katayama, K. Ogawa, H. Ohashi, H. Kimura, S. Takahashi, K. Takeshita, *et al.*, New Journal of Physics **15**, 083035 (2013).
[44]Y. Inubushi, T. Yabuuchi, T. Togashi, K. Sueda, K. Miyanishi, Y. Tange, N. Ozaki, T. Matsuoka, R. Kodama, T. Osaka, *et al.*, Applied Sciences **10**, 2224 (2020).
[45]T. Kameshima, A. Takeuchi, K. Uesugi, T. Kudo, Y. Kohmura, K. Tamasaku, K. Muramatsu, T. Yanagitani, M. Yabashi, and T. Hatsui, Optics letters **44**, 1403 (2019).
[46]T. Kameshima and T. Hatsui, in *Journal of Physics: Conference Series*, Vol. 2380 (IOP Publishing, 2022) p. 012094.
[47]M. Yabashi, H. Tanaka, and T. Ishikawa, Journal of synchrotron radiation **22**, 477 (2015).
[48]H. Yumoto, H. Mimura, T. Koyama, S. Matsuyama, K. Tono, T. Togashi, Y. Inubushi, T. Sato, T. Tanaka, T. Kimura, *et al.*, Nature Photonics **7**, 43 (2013).
[49]T. Pikuz, A. Faenov, T. Matsuoka, S. Matsuyama, K. Yamauchi, N. Ozaki, B. Albertazzi, Y. Inubushi, M. Yabashi, K. Tono, *et al.*, Scientific Reports **5**, 17713 (2015).
[50]H.-S. Park, D. M. Chambers, H.-K. Chung, R. J. Clarke, R. Eagleton, E. Giraldez, T. Goldsack, R. Heathcote, N. Izumi, M. H. Key, *et al.*, Physics of Plasmas **13**, 056309 (2006).
[51]T. Weitkamp, A. Diaz, C. David, F. Pfeiffer, M. Stampanoni, P. Cloetens, and E. Ziegler, Optics express **13**, 6296 (2005).
[52]B. K. Blykers, C. Organista, M. N. Boone, M. Kagias, F. Marone, M. Stampanoni, T. Bultreys, V. Cnudde, and J. Aelterman, Scientific reports **11**, 18446 (2021).
[53]A. Brailovsky, S. Gaponov, and V. Luchin, Applied Physics A **61**, 81 (1995).
[54]X. Bai, T. Wang, Y. Zhu, and G. Luo, World Journal of Mechanics **8**, 94 (2018).
[55]I. Zanette, C. David, S. Rutishauser, and T. Weitkamp, in *AIP Conference Proceedings*, Vol. 1221 (American Institute of Physics, 2010) pp. 73–79.
[56]M. Kagias, Z. Wang, P. Villanueva-Perez, K. Jefimovs, and M. Stampanoni, Physical Review Letters **116**, 093902 (2016).